Appendix: Supplemental material

A Definition of angles

Using the decay $B^0 \to D^{*-}D_{s1}(2460)^+$ as an example and naming the intermediate dipion resonance $R(\pi\pi)$, there are four decays accounted for in the amplitude: $B^0 \to D^{*-}D_{s1}(2460)^+$, $D^{*-} \to \overline{D}^0\pi^-$, $D_{s1}(2460)^+ \to D_s^+R(\pi\pi)$, and $R(\pi\pi) \to \pi^+\pi^-$. Figure S1 shows the definitions of the helicity angles and the angles between two decay planes used to describe the amplitude. The helicity angle of the $B \to D^*D_{s1}(2460)^+$ decay is denoted as θ. The angle between the $D_{s1}(2460)^+ \to D_s^+R(\pi\pi)$ and $D^* \to D\pi$ decay planes is denoted as $\phi_0 = \phi_0^{'} + \phi_0^{''}$. The helicity angles of the $D^* \to D\pi$ and $D_{s1}(2460)^+ \to D_s^+R(\pi\pi)$ decays are denoted as θ_0 and θ_1, respectively. The angle between the $D_{s1}(2460)^+ \to D_s^+R(\pi\pi)$ and $R(\pi\pi) \to \pi^+\pi^-$ decay planes is denoted as ϕ_1, and the helicity angle of the $R(\pi\pi) \to \pi^+\pi^-$ decay is denoted as θ_2.

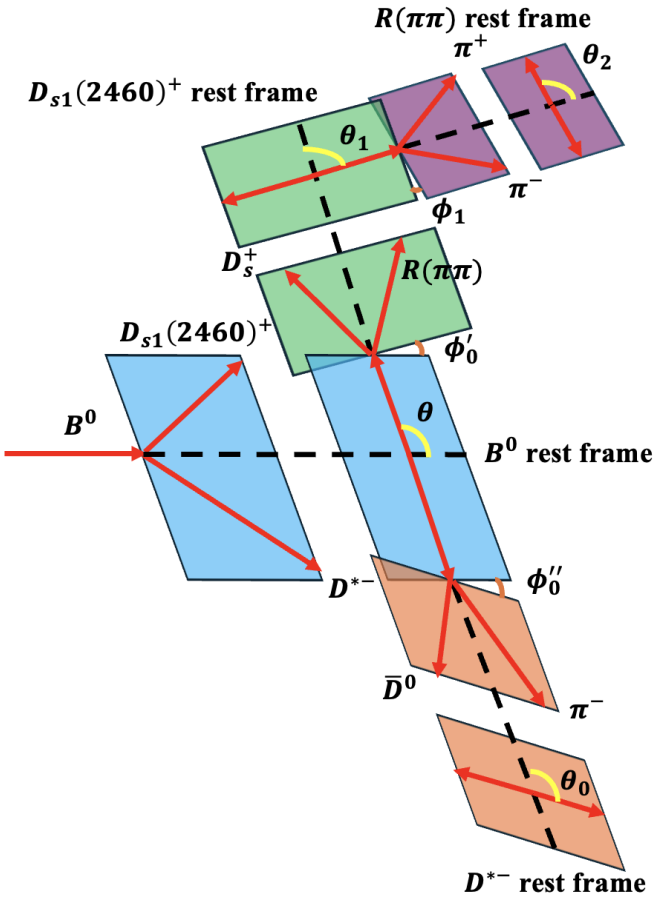

Figure S1: Definitions of the helicity angles for $B^0 \to D^{*-}D_{s1}(2460)^+$ decays, with the intermediate resonance R decaying into $\pi\pi$.

B Data distributions

The efficiency-corrected data distributions combining $B^0 \to D^- D_{s1}(2460)^+$ and $B^+ \to \overline{D}^0 D_{s1}(2460)^+$ channels are shown in Fig. S2. The corresponding distributions for the $B^0 \to D^{*-} D_{s1}(2460)^+$ channel are shown in Fig. S3, while two-dimensional distributions for this channel are shown in Fig. S4.

C Pull distributions

The distributions in the $m^2(\pi^+\pi^-) - m^2(D_s^+\pi^+)$ and $\phi_1 - \cos(\theta_1)$ planes, superimposed on the normalised residual between adaptive binned data and model (pull) for the $f_0(500) + f_0(980) + f_2(1270)$ model, the $f_0(500)+$RBW $T_{c\bar{s}}^{++}$ model, and the $f_0(500)+$K-matrix $T_{c\bar{s}}^{++}$ model, are shown in Figs. S5, S6, and S7, respectively. The adaptive binning is chosen such that each bin contains enough data points, so the χ^2 value can be correctly evaluated.

D Significance test

The 2ΔNLL distribution obtained from pseudoexperiments is shown in Fig. S8, and is fitted with a χ^2 distribution. Given that the 2ΔNLL value from data is 490.4, the significance of two $T_{c\bar{s}}$ contributions is estimated to be much larger than $10\,\sigma$.

E Spin-parity test

The 2ΔNLL distributions obtained from pseudoexperiments are shown in Fig. S9. The blue histogram denotes the distribution obtained from an ensemble of pseudoexperiments generated according to the results of the fit to data with the spin-0 hypothesis, which has a mean consistent with the 2ΔNLL value observed in data (violet line). The red histogram denotes the distribution obtained from a corresponding ensemble with the spin-1 hypothesis, and is fitted with a Gaussian function, the result of which is shown (green line). The difference between the 2ΔNLL value observed in data and the mean value of the spin-1 pseudoexperiments corresponds to a significance of $10\,\sigma$, demonstrating that $J^P = 0^+$ is favoured with high significance.

F Fit plots including interference contributions

The comparisons between data and fit results with different models including the interference contributions are shown in Figs. S10–S12, where the interference contributions are mostly negative.

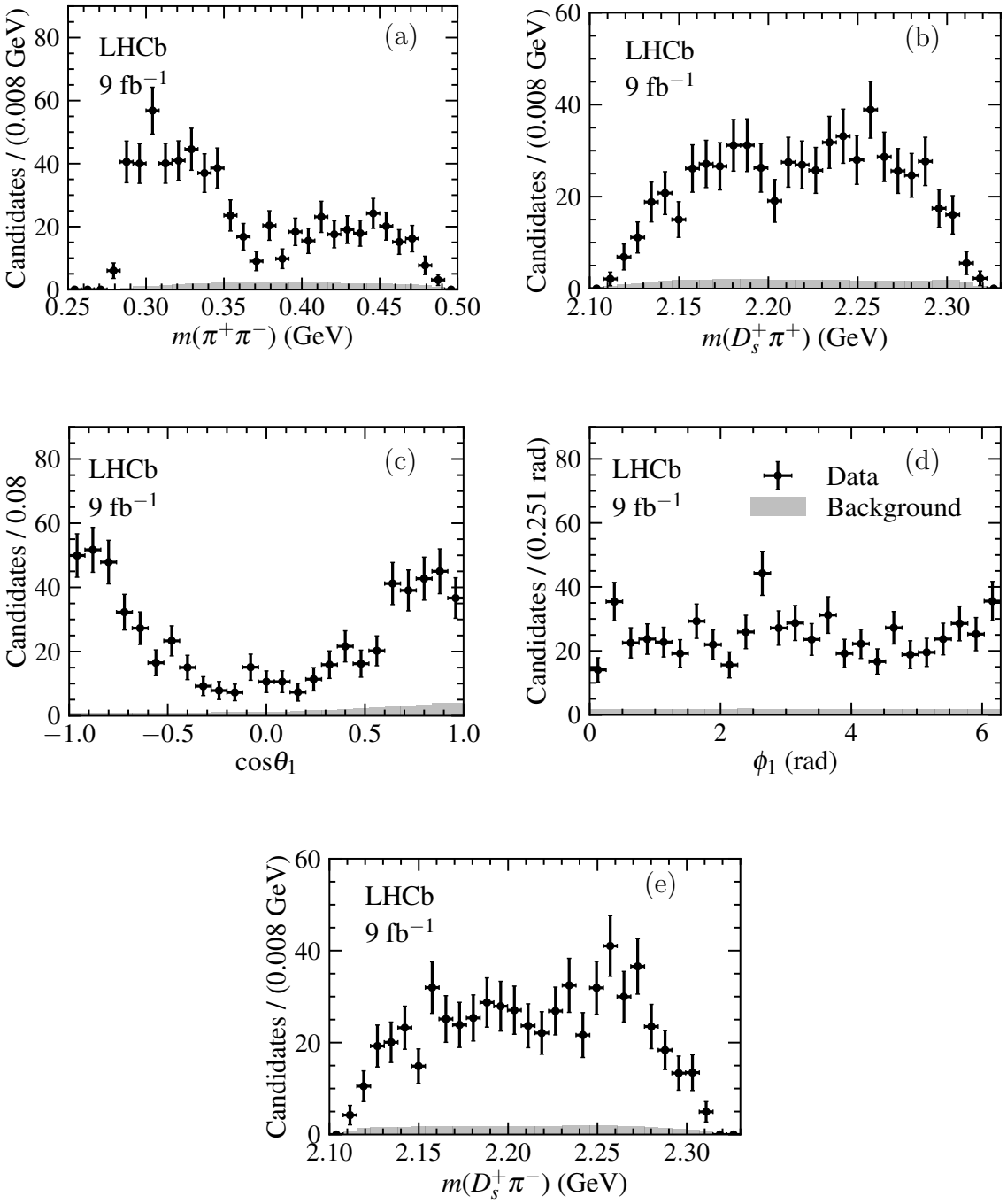

Figure S2: Efficiency-corrected distributions of the $D_{s1}(2460)^+ \to D_s^+\pi^+\pi^-$ phase-space variables including (a) $m(\pi^+\pi^-)$, (b) $m(D_s^+\pi^+)$, (c) $\cos\theta_1$, (d) ϕ_1 and (e) $m(D_s^+\pi^-)$ combining the $B^0 \to D^- D_{s1}(2460)^+$ and $B^+ \to \overline{D}^0 D_{s1}(2460)^+$ channels, where black dots with error bars denote data points and gray histograms denote background.

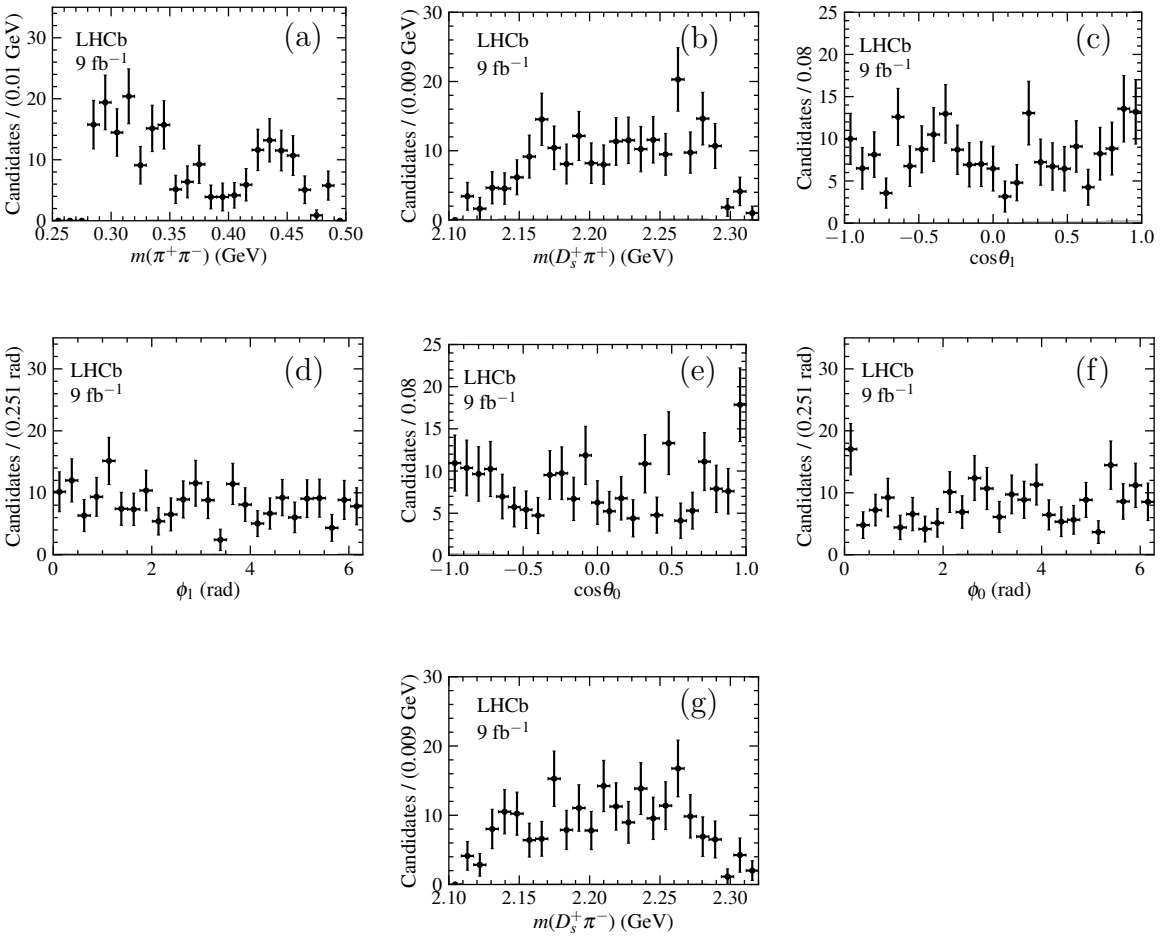

Figure S3: Efficiency-corrected distributions of the $D_{s1}(2460)^+ \to D_s^+\pi^+\pi^-$ phase-space variables including (a) $m(\pi^+\pi^-)$, (b) $m(D_s^+\pi^+)$, (c) $\cos\theta_1$, (d) ϕ_1, (e) $\cos\theta_0$, (f) ϕ_0 and (g) $m(D_s^+\pi^-)$ for the $B^0 \to D^{*-}D_{s1}(2460)^+$ channel, where black dots with error bars denote data points and the background is not shown due to its low contribution.

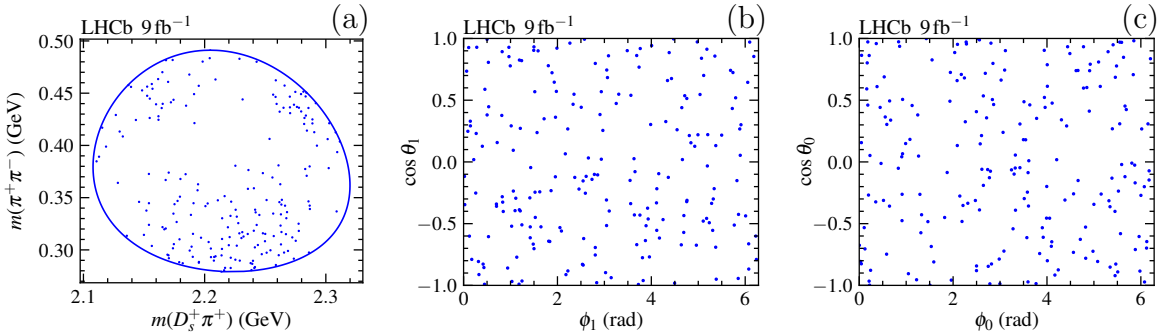

Figure S4: Distributions of selected candidates in the (a) $m(D_s^+\pi^+) - m(\pi^+\pi^-)$ plane, (b) $\phi_1 - \cos\theta_1$ plane and (c) $\phi_0 - \cos\theta_0$ plane for the $B^0 \to D^{*-}D_{s1}(2460)^+$ channel.

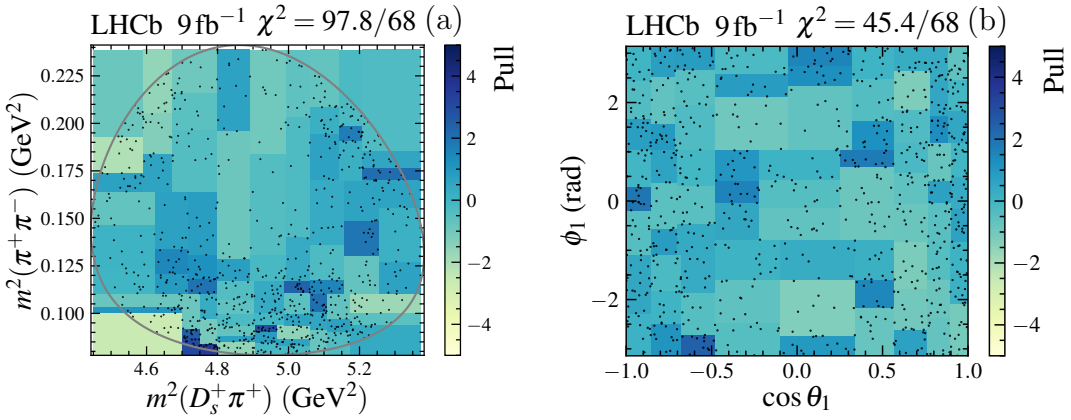

Figure S5: Data distributions in the (a) $m^2(\pi^+\pi^-) - m^2(D_s^+\pi^+)$ and (b) $\phi_1 - \cos(\theta_1)$ planes combining the three signal channels, superimposed on the normalised residuals between adaptive binned data and model (pull) for the $f_0(500) + f_0(980) + f_2(1270)$ model. The gray solid line in (a) denotes the boundary of the $D_{s1}(2460)^+ \to D_s^+\pi^+\pi^-$ Dalitz plot.

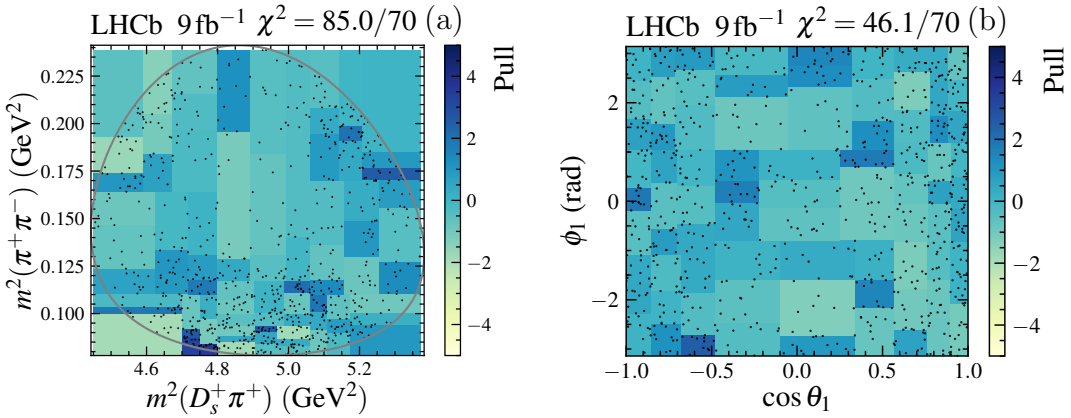

Figure S6: Data distributions in the (a) $m^2(\pi^+\pi^-) - m^2(D_s^+\pi^+)$ and (b) $\phi_1 - \cos(\theta_1)$ planes combining the three signal channels, superimposed on the normalised residuals between adaptive binned data and model (pull) for the $f_0(500) + \text{RBW}\ T_{c\bar{s}}^{++}$ model. The gray solid line in (a) denotes the boundary of the $D_{s1}(2460)^+ \to D_s^+\pi^+\pi^-$ Dalitz plot.

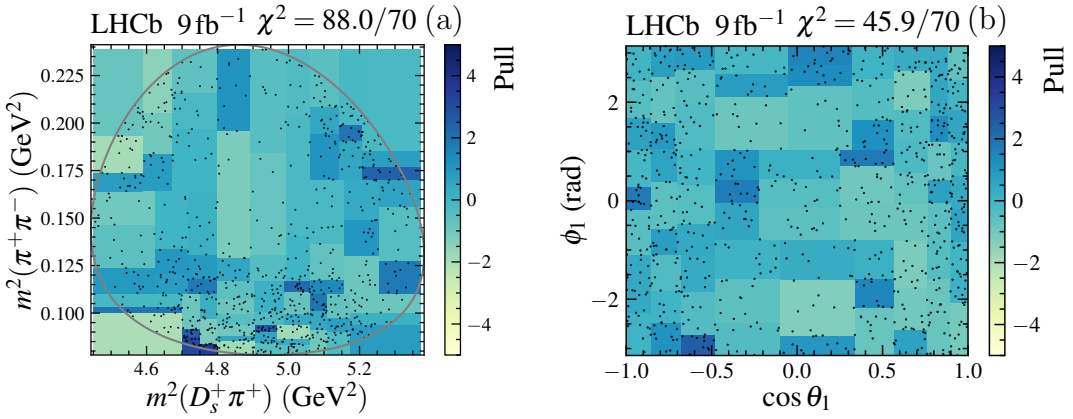

Figure S7: Data distributions in the (a) $m^2(\pi^+\pi^-) - m^2(D_s^+\pi^+)$ and (b) $\phi_1 - \cos(\theta_1)$ planes combining the three signal channels, superimposed on the normalised residuals between adaptive binned data and model (pull) for the $f_0(500) + \text{K-matrix}\ T_{c\bar{s}}^{++}$ model. The gray solid line in (a) denotes the boundary of the $D_{s1}(2460)^+ \to D_s^+\pi^+\pi^-$ Dalitz plot.

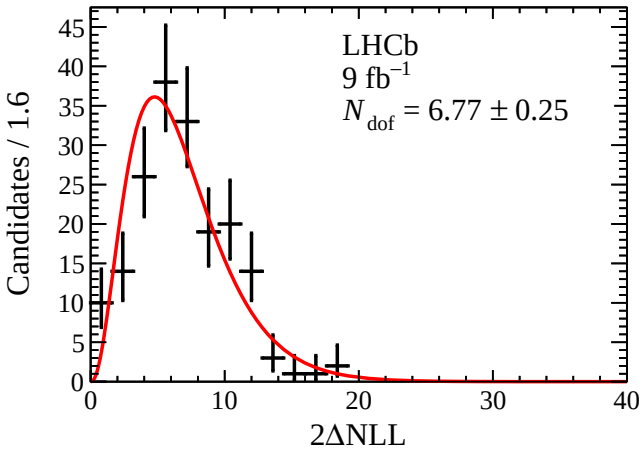

Figure S8: Distribution of 2ΔNLL values used to estimate the significance of two $T_{c\bar{s}}$ contributions, where ΔNLL is the change in negative log likelihood between the fit results with model $f_0(500) + f_0(980)$ and model $f_0(500) + f_0(980) + \text{K-matrix}\ T_{c\bar{s}}$. The 2ΔNLL distribution is fitted with a χ^2 distribution shown as red solid line.

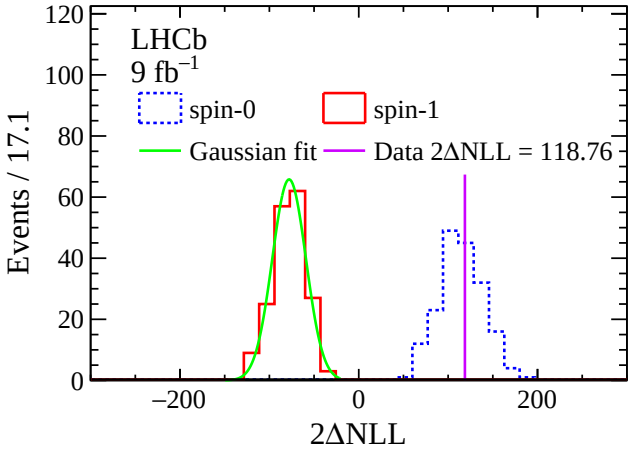

Figure S9: Distributions of 2ΔNLL values used to estimate the significance of the $T_{c\bar{s}}$ spin-parity hypothesis, where ΔNLL is the change in negative log likelihood between the fit results with spin-1 and spin-0 hypotheses.

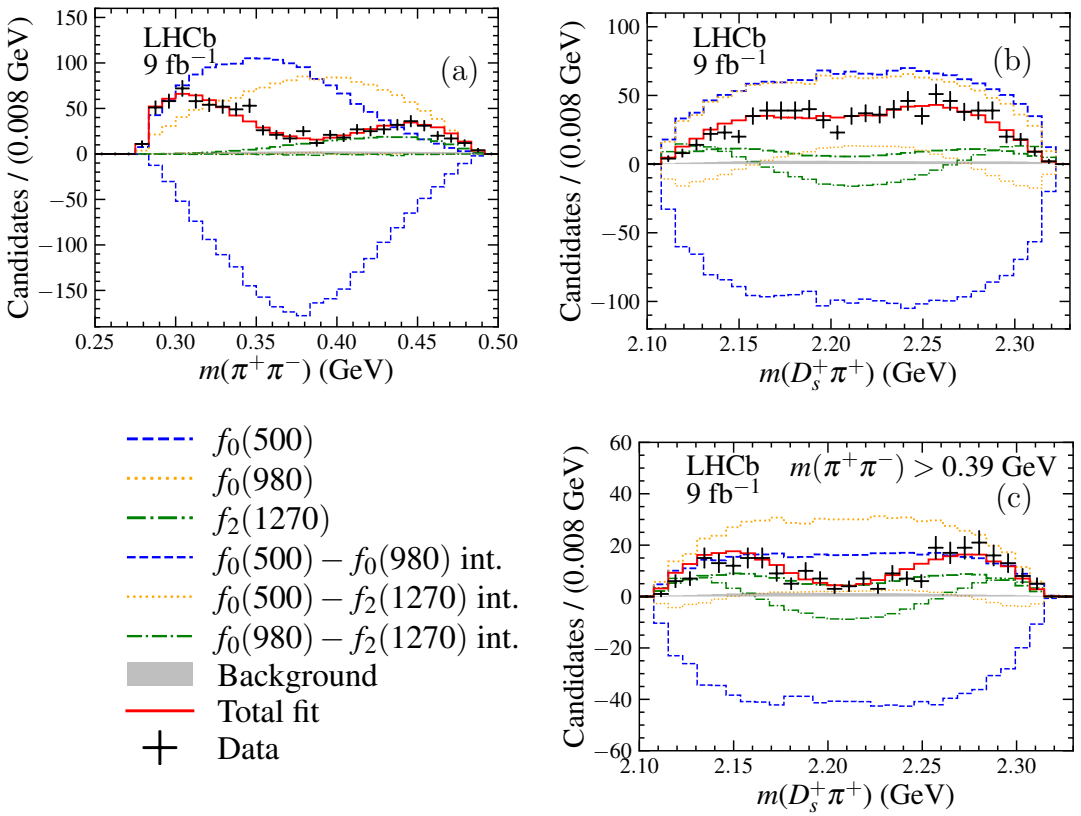

Figure S10: Comparison between data (black dots with error bars) and results of the fit with the $f_0(500) + f_0(980) + f_2(1270)$ model (red solid line). The distributions are for the three channels combined in (a) $m(\pi^+\pi^-)$, (b) $m(D_s^+\pi^+)$, and (c) $m(D_s^+\pi^+)$ requiring $m(\pi^+\pi^-) > 0.39\,\text{GeV}$. Individual components, corresponding to the background contribution estimated by $m(D_s^+\pi^+\pi^-)$ sideband regions (gray-filled) and different contributions from resonances (coloured dashed lines) and interference between the resonances (coloured dotted lines), are also shown as indicated in the legend.

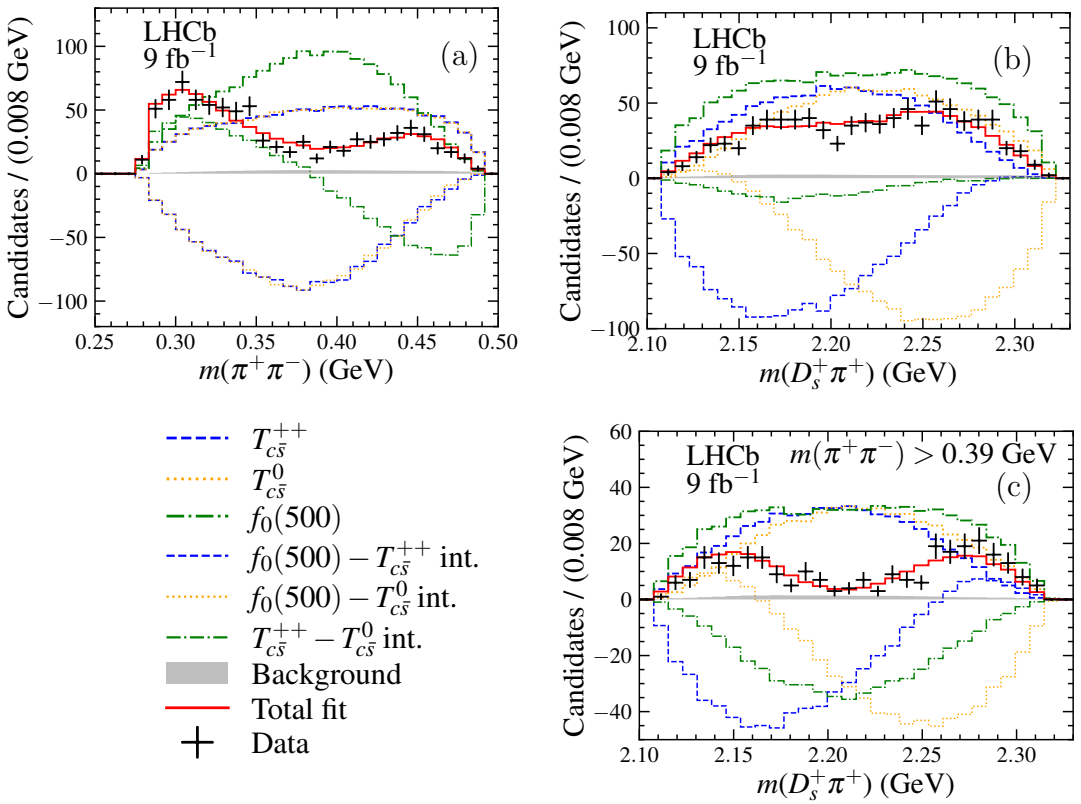

Figure S11: Comparison between data (black dots with error bars) and results of the fit with the $f_0(500) + \text{RBW}\ T_{c\bar{s}}(0^+)$ model (red solid line). The distributions are for the three channels combined in (a) $m(\pi^+\pi^-)$, (b) $m(D_s^+\pi^+)$, and (c) $m(D_s^+\pi^+)$ requiring $m(\pi^+\pi^-) > 0.39\,\text{GeV}$. Individual components, corresponding to the background contribution estimated by $m(D_s^+\pi^+\pi^-)$ sideband regions (gray-filled) and different contributions from resonances (coloured dashed lines) and interference between the resonances (coloured dotted lines), are also shown as indicated in the legend.

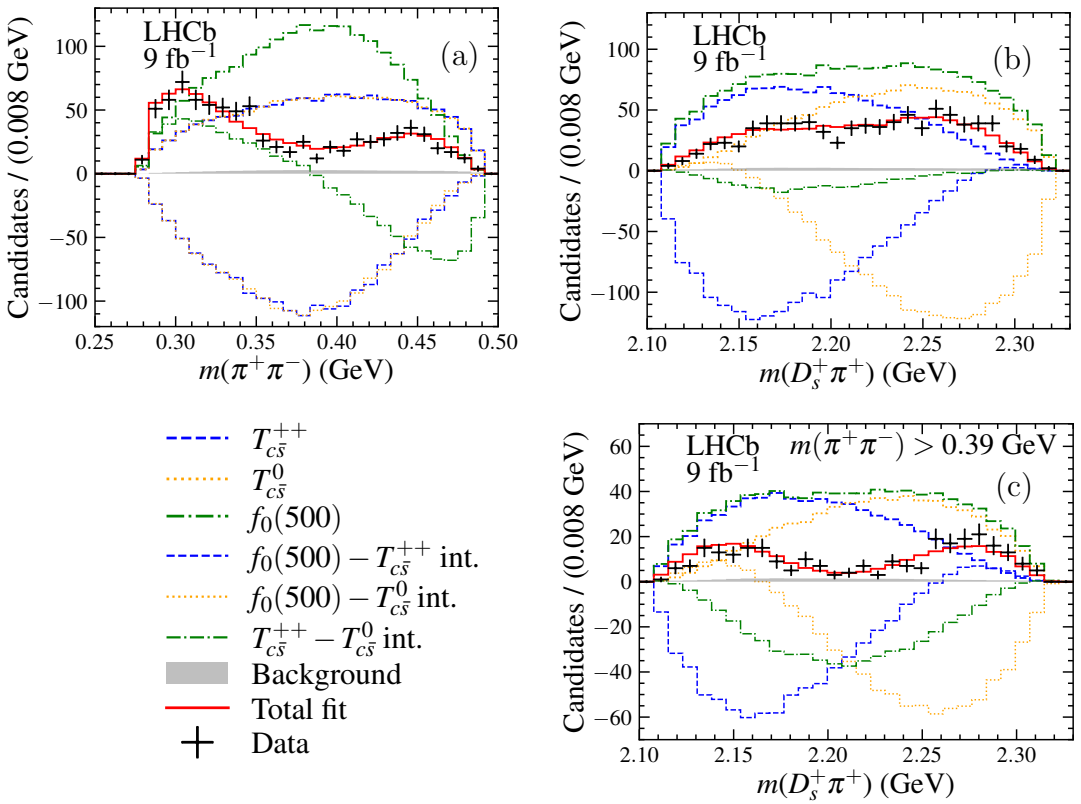

Figure S12: Comparison between data (black dots with error bars) and results of the fit with the $f_0(500)$ + K-matrix $T_{c\bar{s}}(0^+)$ model (red solid line). The distributions are for the three channels combined in (a) $m(\pi^+\pi^-)$, (b) $m(D_s^+\pi^+)$, and (c) $m(D_s^+\pi^+)$ requiring $m(\pi^+\pi^-) > 0.39\,\text{GeV}$. Individual components, corresponding to the background contribution estimated by $m(D_s^+\pi^+\pi^-)$ sideband regions (gray-filled) and different contributions from resonances (coloured dashed lines) and interference between the resonances (coloured dotted lines), are also shown as indicated in the legend.